Final Report for the FY19 FES Theory Performance Target

D. R. Hatch[1], M. T. Kotschenreuther[1], S. M. Mahajan[1], M. Halfmoon[1], E. Hassan[1], G. Merlo[1], C. Michoski[1], J. Canik[2], A. Sontag[2], I. Joseph[3], M. Umansky[3], W. Guttenfelder[4], A. Diallo[4], R. Groebner[5], A. O. Nelson[4], F. Laggner[4], J. Hughes[6], and S. Mordijck[7]

[1]University of Texas at Austin
[2]Oak Ridge National Laboratory
[3]Lawrence Livermore National Laboratory
[4]Princeton Plasma Physics Laboratory
[5]General Atomics
[6]MIT
[7]William and Mary

The FY19 Theory Performance Target

Understanding the relevant turbulent transport mechanisms at the edge of a high-performance tokamak is essential for predicting and optimizing the H-mode pedestal structure in future burning plasma devices. Global electromagnetic gyrokinetic simulations will be performed based on representative experimental pedestal scenarios in order to clarify which instabilities are most important for each of the particle and heat transport channels. Edge transport modeling will be performed in order to estimate and bound the particle and heat sources—e.g., the ionization density source and the atomic energy loss channels due to ionization, charge exchange, and radiation. Comparisons will be made with data from the DIII-D, JET, C-Mod and NSTX or MAST experiments.

1 Executive Summary

Transport barriers form at the edge of fusion plasmas when turbulence is suppressed by sheared flows. The resulting pedestal—the narrow region with steep pressure gradients—drastically boosts plasma confinement and will be, perhaps, the largest determining factor in making the final step to high fusion gain. ITER, for example, is designed to exploit an edge

transport barrier to achieve its goals. This boon to fusion energy, however, is accompanied by challenges and uncertainties in the transition to burning plasmas. ITER will rely not only on accessing a pedestal, but on the pedestal achieving a sufficient temperature at its inner boundary (thought to be in the range of 4 keV). Moreover, edge transport barriers often produce edge localized modes (ELMs)—explosive MHD events that cyclically collapse the pedestal, threatening plasma facing components. The residual turbulent transport in the pedestal is central to determining pedestal structure and the accessibility and properties of ELM-free regimes. The goal of the FES FY19 theory performance target (TPT) was to develop a deep understanding of the turbulent transport mechanisms, along with the corresponding heat and particle sources, that govern pedestal dynamics. This was accomplished via two sets of computational tools: (1) gyrokinetic codes (GENE [1, 2] and CGYRO [3]), which can analyze the instabilities and transport that arise in the pedestal, and (2) edge codes (SOLPS and UEDGE), which can provide the best possible estimate of particle and heat sources. Comparisons have been made with experiments spanning several devices and exploring a wide range of parameters and modes of operation. This final report provides an overview of FY19 TPT. Major conclusions are as follows:

- Edge transport barriers typically lie in a regime in which heat diffusivity far exceeds particle diffusivity: $D_e/\chi_e \ll 1$.
- ETG and MTM are important mechanisms for electron heat transport and one or both will generally be major contributors to χ_e.
- In addition to its transport signature, which is consistent with $D_e/\chi_e \ll 1$, MTM activity is further established, perhaps incontrovertibly, by the close quantitative agreement between distinctive bands in magnetic spectrograms and corresponding bands of unstable MTM in gyrokinetic simulations. This is now established over several discharges.
- Neoclassical transport in both electron particle and ion heat channels is consistently at levels that are not negligible, but remains somewhat smaller than edge modeling predictions.
- MHD modes, if active, cannot simultaneously account for all transport in both particle and heat channels and in fact their main impact must be limited to the particle channel.
- ITG and ETG are observed in some cases to produce pinch velocities of up to $\sim 0.2 m/s$ (attributing all flux to pinch and no diffusion).
- Neoclassical, MTM, ETG, and ITG can all produce relevant electron particle transport levels (the latter two in either positive or negative directions). Within uncertainties, they can plausibly account for all particle transport. Generally, however, these mechanisms are found to collectively produce particle transport somewhat below the edge modeling predictions. This suggests that an additional particle transport mechanism, like KBM, may be necessary.

This combined analysis of instabilities / transport and edge modeling is unprecedented and, having been applied to a wide range discharges and devices, has qualitatively advanced our understanding of pedestal transport. Such an understanding is necessary to predict and optimize pedestals in future burning plasma devices.

2 Introduction

Following a half century of extraordinary progress in plasma magnetic confinement via tokamaks, with, for example, the fusion triple product increasing at a rate surpassing Moore's law, magnetic confinement finds itself poised on the brink of high fusion gain. The narrow transport barrier that forms at the edge of an H-mode fusion plasma will, perhaps, be the largest determining factor in making the final step to a burning plasma. This transport barrier arises when the conventional plasma turbulence mechanisms are suppressed by sheared flows. This allows a pedestal—a region of steep pressure gradients—to form, drastically boosting the plasma confinement. ITER, and nearly all other prospective burning plasma devices, are designed to exploit edge transport barriers to achieve their goals.

This boon to fusion energy, however, is accompanied by challenges and uncertainties that must be dealt with in the transition to burning plasma experiments. ITER, for example, will rely not only on accessing a pedestal, but on the pedestal achieving a sufficient temperature at its inner boundary (thought to be in the range of 4 keV). Moreover, edge transport barriers often produce edge localized modes (ELMs)—explosive MHD events that cyclically collapse the pedestal. ELMs are tolerable on present day experiments but will release unacceptable heat loads on the plasma-facing components of burning plasma devices.

There are also many opportunities for innovation and optimization. Many promising solutions to the ELM problem have been identified. I-mode [4] and wide pedestal QH-mode [5], for example, naturally produce edge transport barriers without the damaging ELMs. External coils inducing resonant magnetic perturbations (RMPs) in the plasma can also produce ELM-free pedestals. These ELM free regimes rely on some transport mechanism to arrest the development of the pedestal away from MHD limits. Another scenario, the Super-H mode, exploits a deep understanding of MHD stability limits to achieve unprecedented pedestal pressures. Though promising, it remains an open question how these innovative modes of operation will extrapolate to reactor parameters.

Considering both the hazards (e.g. ELMs) and uncertainties on one hand, and the possibilities for innovation and optimization on the other hand, edge transport barriers surely represent simultaneously some of the greatest challenges *and* opportunities for fusion energy.

The properties of an edge transport barrier are governed by three complex and sensitively interconnected components: (1) pedestal MHD stability, (2) divertor and SOL conditions, and (3) the residual transport (along with corresponding sources and sinks) in the edge transport barrier.

Of these three, MHD stability is likely the best understood and is widely used to interpret and predict pedestal structure [6]. The pre-ELM pedestal pressure is typically observed to lie near the peeling ballooning stability boundary, and ideal MHD has been successful at describing the ultimate pressure limit of the pedestal. In a standard type-I ELMy H-mode, the edge profiles evolve until a peeling ballooning (ideal MHD) stability limit is reached, triggering an ELM crash. An ELM crash produces a rapid ejection of plasma pressure (typically 5% and up to 20% of the stored energy), at which point the profiles rebuild and the cycle repeats. It is useful to conceptualize pedestal structure and evolution in terms of the width and height of the pedestal pressure, the pre-ELM pedestal height being the parameter that quantifies the quality of the discharge. A peeling-ballooning instability is triggered,

roughly speaking, when the pedestal pressure gradient surpasses a critical value. Although this is useful information, it has little predictive power, since any number of values for the pedestal top pressure are acceptable given a sufficient pedestal width. A second constraint is provided by the transport mechanisms operative in the pedestal. These transport processes, in conjunction with the peeling-ballooning stability constraint, ultimately determine the pre-ELM pedestal structure. Models like EPED [6] appeal to the stability limit for the kinetic ballooning mode (KBM) for the second constraint. Such models have provided a valuable conceptual framework and have been quite successful in describing pedestal properties in the standard regimes of present-day experiments.

However, many important problems lie outside (either partially or fully) the scope of EPED-like models. For example, metal wall experiments (e.g., JET, with its strong constraint on pedestal temperature [7]) demonstrate the need to understand the extra demands on heating power and self-consistently capture the separate dynamics of the density and temperature profiles. Moreover, ELM-free regimes (e.g., I-mode, QH-mode, ELM-suppressed RMP scenarios, etc.) by definition do not surpass an ELM-triggering peeling-ballooning threshold and so lie beyond the realm of applicability for EPED. As may be expected, pedestal structure is extremely difficult to predict for these ELM-free regimes. Ultimately a deep understanding of pedestal transport and the related sources/sinks is necessary in order to achieve true predictive capability throughout the broad range of prospective edge transport barriers that must be explored for ELM-free operation on ITER or other burning plasma devices.

Consequently, the residual transport in the edge transport barrier is a critical area of research and yet it remains, perhaps, the least understood component of the edge system. Transport, in combination with the corresponding sources and sinks, determines the heating power necessary to achieve a given pedestal temperature; the inter-ELM evolution of pedestal density and temperature profiles, which ultimately determines the operating point at which an ELM is triggered; and the accessibility and properties of ELM-free regimes. An understanding of pedestal transport is indispensable to tokamak design, optimization, and operation.

The goal of this theory performance target is to identify the turbulent transport mechanisms, along with the corresponding heat and particle sources, that govern pedestal dynamics. This will be accomplished via two sets of computational tools: (1) gyrokinetic codes (GENE and CGYRO), which can analyze the instabilities that arise in the pedestal, and (2) edge codes (SOLPS and UEDGE), which, when operated in interpretive mode, can provide the best possible estimate of particle and heat sources—e.g., the ionization density source and the atomic energy loss channels due to ionization, charge exchange, and radiation. SOLPS and UEDGE approach the same problem using different models (e.g. treatment of neutrals) and algorithms and so will provide complementary information regarding the sensitivity of the results to model assumptions and uncertainties. Comparisons have been made with experiments spanning several devices and exploring a wide range of parameters and modes of operation.

This TPT complements the concurrent joint research target (JRT), which is focused on understanding the relative role of sources and transport in determining the structure of the density pedestal. Multiple DIII-D discharges have been jointly analyzed within the TPT and the JRT.

This report is outlined as follows. Sec. 3 reviews some basic considerations of the prospective transport mechanisms. Sec. 4 introduces the experimental discharges studied in the TPT. Sec. 5 gives an overview of the edge modeling results. Sec. 6 describes the gyrokinetic simulations and summarizes the resulting transport predictions. Major results are summarized in Sec. 8.

Table 1: Description of discharges selected for the FY19 TPT, spanning many operational scenarios and devices.

Device	Discharge #	Type	Description
DIII-D	153764	ELMy H-mode	Study of magnetic fluctuations
DIII-D	162940	ELMy H-mode	Study of particle sources
DIII-D	163518	Wide Pedestal QH-Mode	ELM-free
DIII-D	174082	ELMy H-mode	Baseline discharge in fueling scan
DIII-D	174092	ELMy H-mode	High-pellet case in fueling scan
C-Mod	1120907032	I-mode	ELM-free
NSTX	129038	ELM-free	Lithium-conditioned divertor
JET	92432	ELMy H-mode	Study of ITER-like wall

3 Transport Fingerprints

Plasma profile evolution is governed by conservation laws (i.e., transport equations) for the temperature, density, and momentum of each species. These laws define the response of the profile to fluxes and sources, as illustrated, for example, in the continuity equation. The complete picture involves such equations for the density, temperature, and momentum of electrons, main ions, and impurity species. The focus of this TPT is on the most important subset of these channels, namely the density and temperature of electrons and main ions, which directly determine the confinement of energy. The relative sources for the different channels are controlled by very different mechanisms. The plasma temperature is maintained by outward flux from the core; particle sources include ionization of neutral particles from the edge and, possibly, a turbulent particle pinch; and impurities are drawn in from the edge by a neoclassical pinch.

As may be expected from such different mechanisms, the drive for the different channels also varies widely in magnitude. A useful dimensionless metric for quantifying the drive of the various channels is the ratios of their effective diffusivities (for example D/χ, where $D = \Gamma/\nabla n$, $\chi = Q/(n\nabla T)$, Γ is the particle flux, Q is the heat flux, n is the density, and T is the temperature). The use of effective diffusivities in this manner assumes neither the absence of pinches nor the absence of nonlocal effects, but is, rather, a convenient measure of the gradient that can be supported by a given flux or source. These relative drive quantities are difficult to determine experimentally but can be estimated by interpretive edge modeling. In the cases where this has been done, the electron heat diffusivity typically greatly exceeds the effective particle diffusivity. The edge modeling component of this TPT has greatly expanded the parameter space over which such analyses have been carried out.

The contributors to pedestal transport must be consistent with the general picture outlined above. For example, each prospective transport mechanism has a distinctive transport 'fingerprint' [8] defined by its relative impact on various transport channels, mode frequencies, susceptibility to shear flow, and spatial scales of fluctuations. A minimum subset of pedestal transport mechanisms must include KBM (or similar MHD-like modes), ITG (or similar ion scale electrostatic modes), ETG, MTM, and neoclassical transport. Paleoclassical transport [18] has also been proposed as a pedestal transport mechanism but remains controversial [19]. ETG and MTM affect almost solely the electron heat channel and produce negligible particle transport. ITG (and other ion scale electrostatic modes like TEM) is more versatile, producing substantial ion heat transport and potentially producing inward, outward, or small (balanced pinch and diffusion) particle transport. MHD-like instabilities produce roughly equal diffusivities in all channels. Consequently, the role of such modes can be strongly constrained by the degree to which the various diffusivities are separated in magnitude. For example, if the electron heat diffusivity, greatly exceeds the effective particle diffusivity, this places an upper bound (i.e. the magnitude of the particle diffusivity) on the contribution of an MHD-like mode to the electron heat transport.

4 Description of Discharges

A wide range of experimental discharges has been selected for the FY19 TPT. These discharges have been selected to explore several phenomena of interest, including (1) ELM-free regimes (I-mode and QH-mode), (2) the unexpected impact of an ITER-like metal wall on the JET pedestal, (3) the impact of variations in particle sources, (4) pedestal transport in a spherical tokamak, and (5) magnetic fluctuations observed in standard ELMy H-mode. The discharges are summarized and briefly described in table 1.

Two ELM-free regimes will be analyzed. The I-mode is a naturally ELM-free mode of operation that is defined by a robust temperature pedestal, no corresponding density pedestal, and low impurity confinement. Consequently, it remains ELM free while avoiding the impurity retention that plagues many ELM free scenarios. Due to these favorable properties, I-mode is proposed as an ideal mode of operation for SPARC. Recent gyrokinetic analysis of C-Mod shot #1120907032 has identified ETG turbulence, which accounts for the bulk of the heat transport, and impurity-branch ITG modes, which can account for the particle and impurity transport.

DIII-D discharge #163518 is a so-called wide pedestal QH mode, in which pedestal fluctuations broaden the pedestal, providing access to high pressure while keeping the profiles away from ELM limits.

The magnetic fluctuations in DIII-D discharge #153764 [9] are composed of distinct frequency bands that arise in the inter-ELM cycle and correlate with the saturation of the electron temperature profile. Gyrokinetic analysis has recently connected these magnetic fluctuations with MTM [8]. Edge modeling has determined that the combined transport from ETG and MTM is consistent with the underlying particle sources in the pedestal.

Three DIII-D discharges (162940, 174082, and 174092) are targeted at understanding the role of variations in particle sources in the pedestal. These discharges exploit different divertor configurations (162940) and a scan in pellet fueling (174082, 174092) to vary the

pedestal particle source. These discharges are also being studied within the JRT.

Since installation of an ITER-like wall (tungsten divertor and beryllium wall) on JET, the pedestal temperature has been severely limited, sometimes causing a degradation of confinement [10]. A major operational constraint is the necessity for gas fueling in order to mitigate tungsten sputtering. Gyrokinetic analysis of discharge #92432 identifies ETG and ITG as major transport mechanisms and elucidates many of the trends observed on JET [7]. Kinetic ballooning modes are identified in the local (but not global) linear simulations. Within the TPT, we have analyzed the particle transport.

The role of particle recycling and pedestal fueling has also been studied on NSTX, where lithium conditioning of the lower divertor was used to modify the recycling level during H-mode plasmas. The resulting modification of fueling profiles and pedestal structure, along with linear gyrokinetic analysis has been performed, identifying ETG as a possible mechanism related to the pedestal changes observed with lithium.

5 Overview of Edge Modeling

As discussed above, the relative magnitude of the transport channels (heat and particles) places a strong constraint on pedestal transport mechanisms. In order to exploit this insight, one needs to quantify the edge particle source. To this end, interpretive edge modeling has been undertaken with SOLPS and UEDGE. SOLPS and UEDGE approach the same problem using different models (e.g. treatment of neutrals) and and algorithms and so provide complementary information regarding the sensitivity of the results to model assumptions and uncertainties. In the analysis described here, an iterative scheme is used that adjusts the cross-field transport, modifying the radial profiles of D, χ_e, and χ_i such that the calculated midplane profiles of the density and temperature agree with those measured (transport coefficients are assumed constant in the poloidal direction) [11].

SOLPS was used for DIII-D 153764, DIII-D 162940, DIII-D 174082, DIII-D 174092, and NSTX 129038, and UEDGE was used for DIII-D 162940, DIII-D 163518, and C-Mod 1120907032. Note that both UEDGE and SOLPS were used for DIII-D 162940 (an upper single-null discharge with 4 MW of heating power) as a benchmarking exercise. In the following subsections, we focus on the edge modeling of this discharge in order to illustrate the interpretive edge modeling workflow and its sensitivites and uncertainties.

5.1 Interpretive Modeling with SOLPS and UEDGE

The SOLPS suite of codes [13] couples the B2.5 fluid plasma transport code [14] with the Monte Carlo code EIRENE [15]. Here we use the SOLPS-ITER version of the code [16]. Plasma transport is modeled as classical parallel to the magnetic field (with some corrections for kinetic effects), and ad-hoc transport coefficients are specified by the user to govern transport across flux surfaces. Modified tanh fits to the experimental profiles are used as targets in the iterative fitting scheme, yielding good matches to the pedestal and scrape-off-layer profiles at the midplane. This workflow can be extended further by using divertor measurements (e.g., ion and heat flux profiles) to constrain, for example, the upstream separatrix temperature.

The SOLPS grid covers spatially from just inside the pedestal ($\psi_N \sim 0.9$) into the SOL; this is sufficient to capture the ionization of neutrals within the pedestal that are originated via recycling at the divertor plates. At the core boundary of the simulation, the ion flux corresponding to the neutral beam particle fueling is imposed; pumping is imposed at the entrances to the cryo ducts via a recycling coefficient of $R = 0.5$ (appropriate for the DIII-D pumping systems, where the pumping speeds and conductance out of the plenum are roughly balanced). The iterative scheme is then employed to adjust cross-field transport coefficients to match measured density and temperature profiles.

In UEDGE, the plasma is also described by time-dependent 2D plasma fluid equations that include equations for density, velocity, ion temperature, electron temperature, electrostatic potential. Enhanced efficiency is achieved by using a continuum fluid model of neutral gas, rather than a particle-based kinetic model. While this model improves accuracy in short neutral mean-free path regions of the domain, it reduces accuracy in the long neutral mean-free path regime regions. Thus, it is important to compare the differences in the results obtained between the two codes in order to quantify the sensitivity of the results to the underlying assumptions.

Classical transport is assumed along magnetic field lines, and anomalous transport is assumed across field lines. A finite-volume differencing algorithm is used, and a fully implicit numerical algorithm is used that allows both Newton-like iterations to steady state and time-dependent solutions with large time-steps. In this study, the following simplifications have been made: (1) drifts and currents are not included, and (2) impurity ions and impurity radiation are not included. Including this physics is probably not critical for the present studies focused on penetration of neutral gas into the pedestal region.

The resulting 2D fueling profiles for DIII-D discharge 162940, are shown in Figs. 1, 2 for SOLPS and UEDGE, respectively. These fueling profiles are integrated poloidally to give the radial profile of the ion flux (assuming steady state), which is due to a combination of neutral beam fueling and recycling from the walls. The corresponding heat and particle diffusion coefficients from both codes are shown in Fig. 3 showing good agreement between the codes.

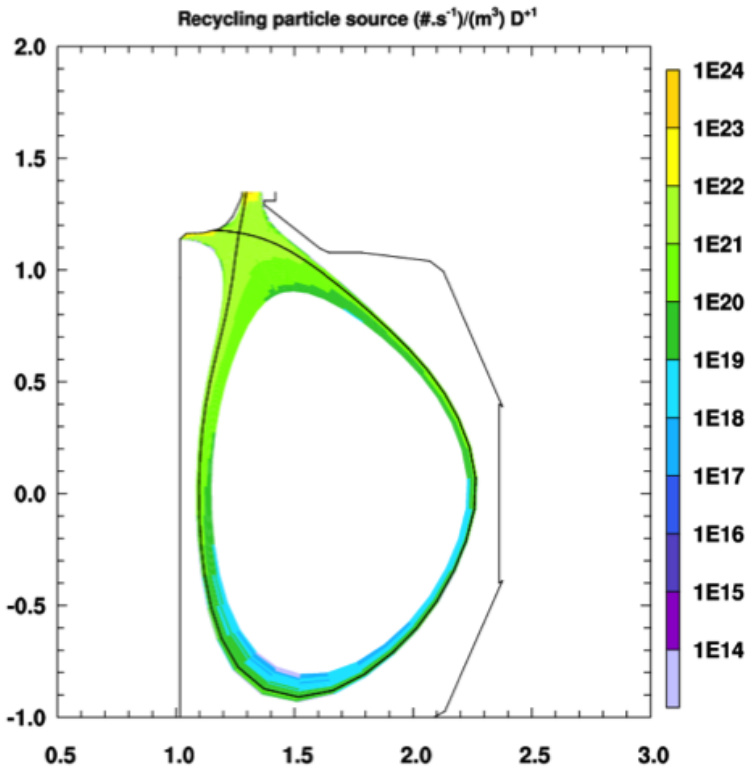

Figure 1: The 2D profiles of the particle source for DIII-D discharge 162940 as calculated with SOLPS.

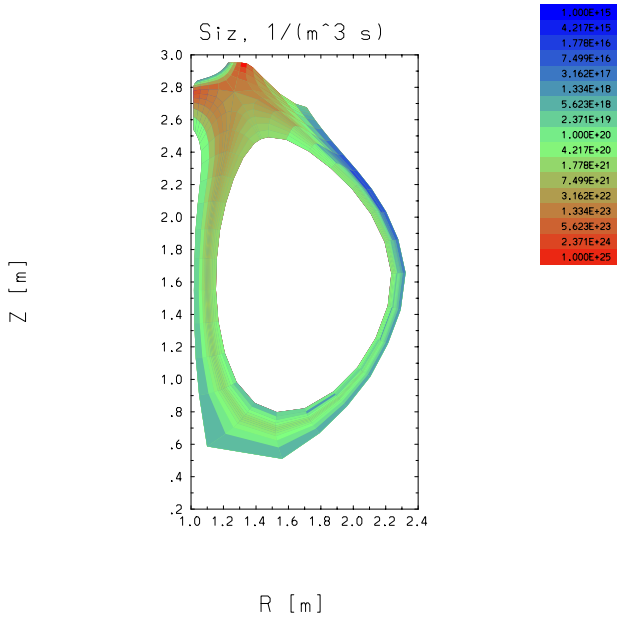

Figure 2: The 2D profiles of the particle source for DIII-D discharge 162940 as calculated with UEDGE.

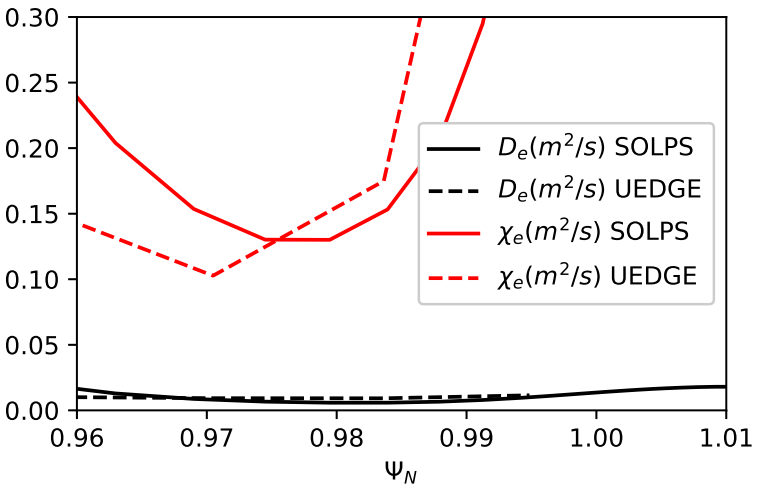

Figure 3: Benchmark of D and χ between SOLPS and UEDGE for DIII-D discharge 162940.

5.2 SOLPS Sensitivity Tests

In order to gauge the sensitivity of results, several tests were carried out via a large set of SOLPS simulations with several variations in the run setup.

First, SOLPS was run on a 'base' case using the tanh profile fits directly. Subsequently, another case was studied where all upstream profiles were shifted outwards an increment of $\Delta\psi_N = 0.005$. The reason for this is that the base case results in an ion flux at the divertor that is lower in SOLPS than is measured by Langmuir probes. By shifting the midplane profiles outwards, the temperature and density at the separatrix are increased and so the divertor fluxes are larger. This directly affects the neutral recycling source, offering a first look at how sensitive the calculated ionization and inferred transport rates are.

Additional variations were motivated by the known difficulty in getting 2D fluid codes to match the ion flux and electron temperature in the inner divertor, which can substantially alter the core fueling characteristics [17] since the inner divertor tends to be very low temperature in experiments, which can offer an easy path to the pedestal without strong ionization of neutrals in the divertor. The variations performed were a) increasing the chemical sputtering yield substantially ($\sim \times 10$) to force the inner leg to a low temperature regime, and b) setting the heat fluxes core boundary condition such that electrons carry 80% of the total power into the SOL (compared to the baseline assumption of an even split between ions and electrons).

The last case is motivated by core interpretive analysis which suggests that ion heat transport is near neoclassical, which is estimated to be 20% of the total power flow. In most cases simulations were performed both assuming pure deuterium plasmas and with companion calculations including carbon produced via sputtering at the wall surfaces. The resulting midplane profiles of electron density and temperature are shown in Fig. 4, illustrating the good fits to the data across all the sensitivity tests.

The modeled and measured profiles of the ion flux to the inner and outer divertors is shown in Fig. 5. Several of the SOLPS simulations match the ion flux at the outer divertor quite well. In the inner divertor, the ion flux shows a secondary peak away from the strike point position, which is not well-captured. Likewise, many of the simulations agree quite well with the measured electron temperature at the outer divertor (Fig. 6), while for the most part SOLPS produces higher temperatures than are measured at the inner divertor. However, the cases with artificially increased sputtering on the inner divertor show good agreement. Overall, the SOLPS simulations achieve the goal of bracketing the measured data across the set of runs and so should give a reasonable range of uncertainty in the final fueling profile calculations.

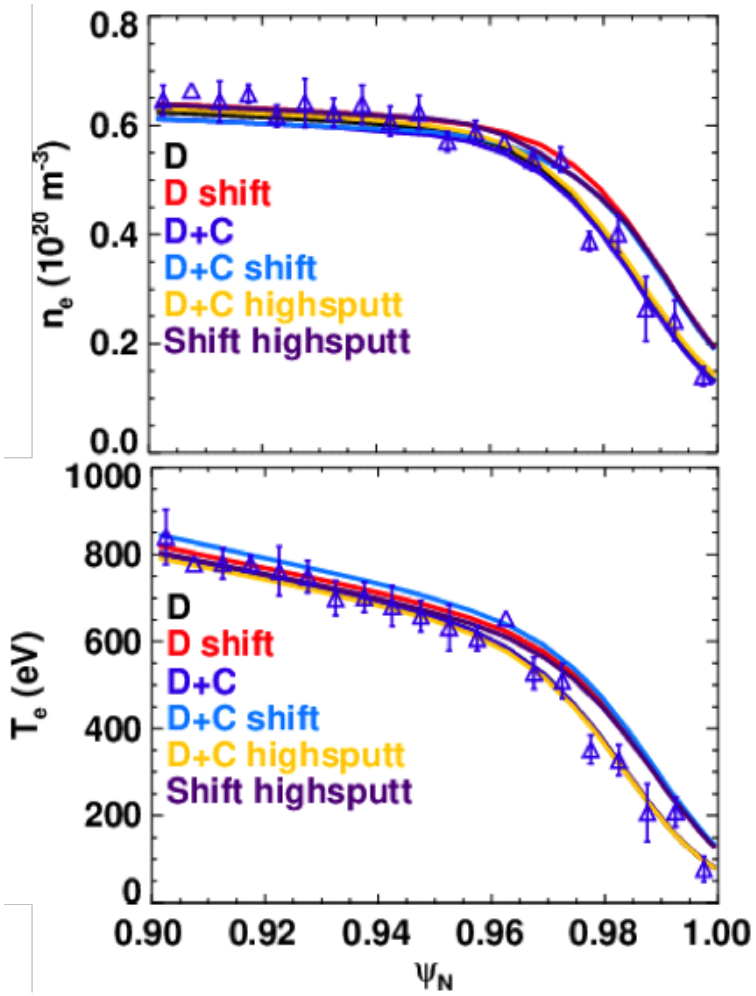

Figure 4: Pedestal density and temperature profiles for DIII-D discharge 162940 along with the matched profiles achieved in the interpretive modeling workflow. The various SOLPS profiles represent variations in the run setup for the purposes of gauging sensitivies.

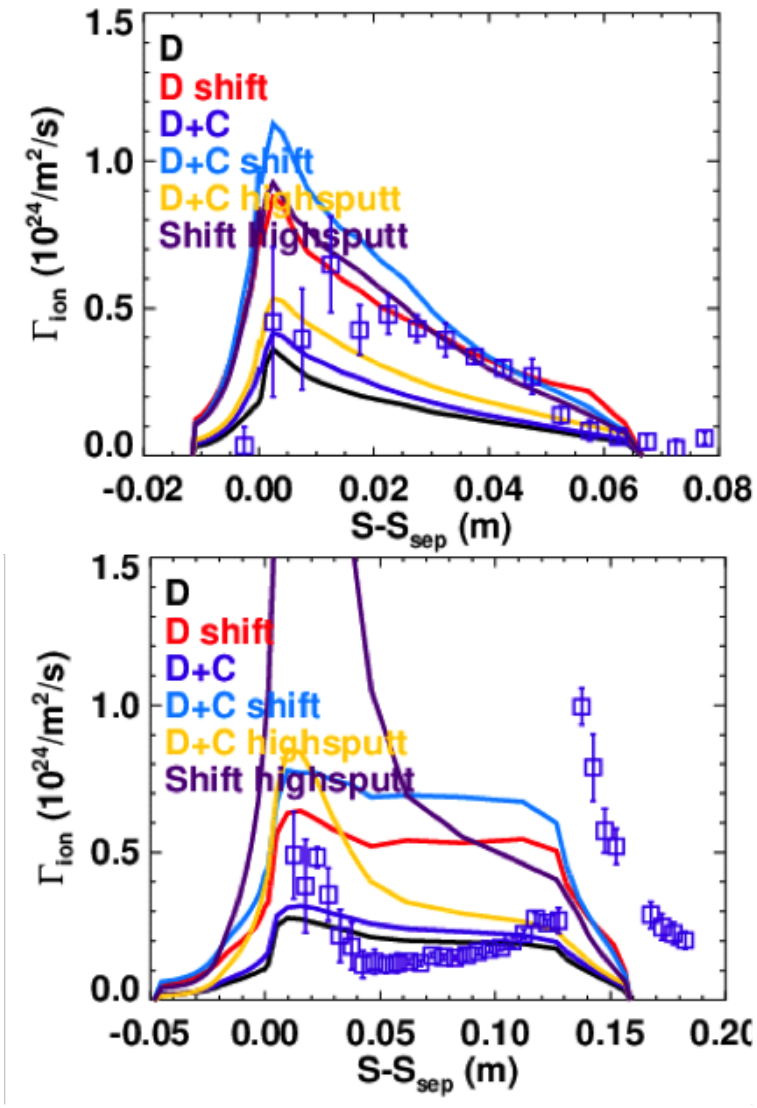

Figure 5: Measured (symbols) and modeled (lines) ion flux to the a) outer and b) inner divertor for discharge 162940.

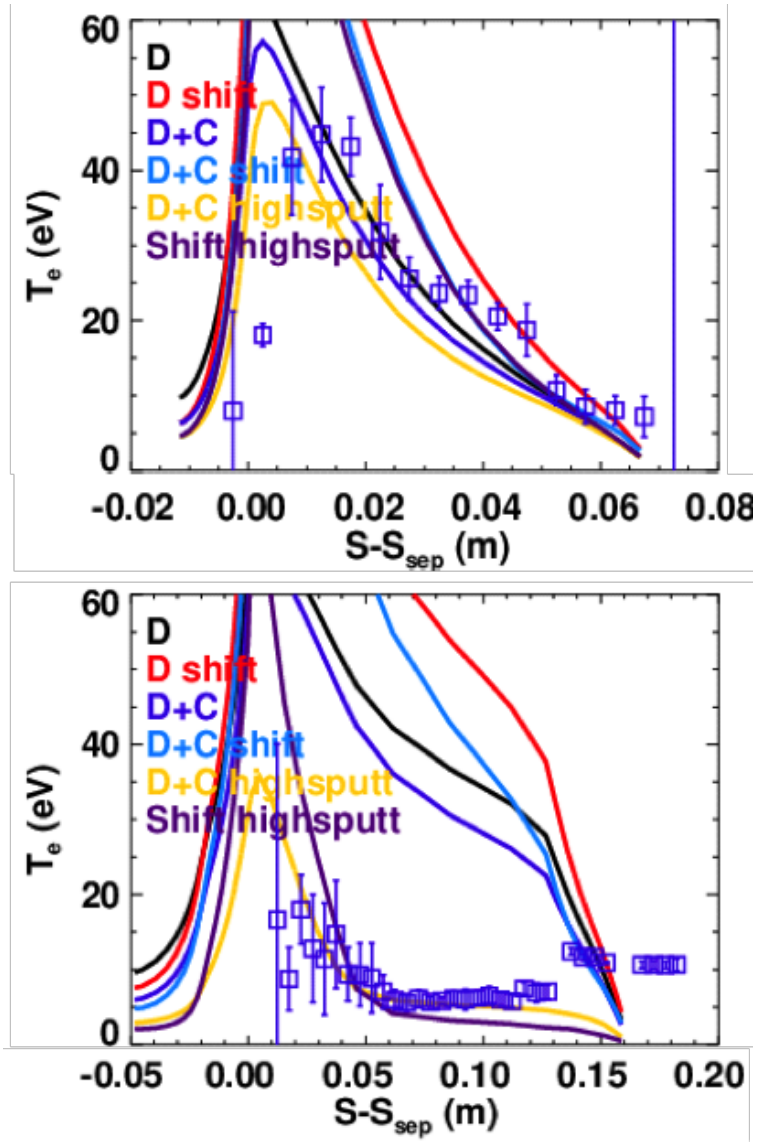

Figure 6: Measured (symbols) and modeled (lines) electron temperature at the a) outer and b) inner divertor for discharge 162940.

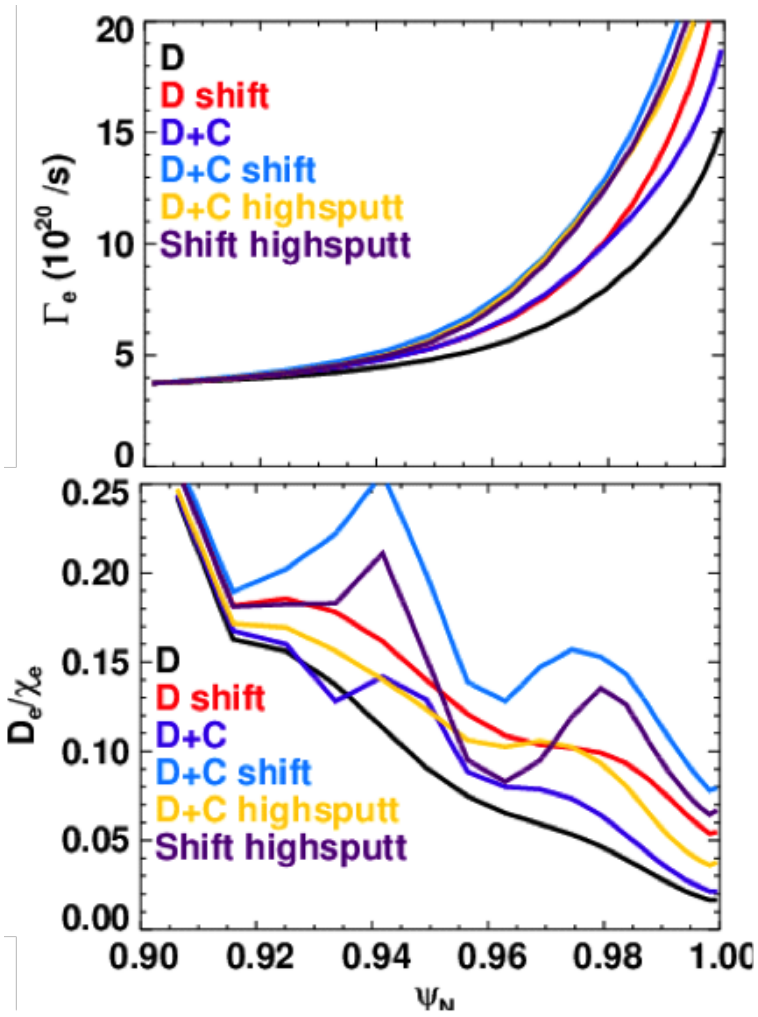

Figure 7: Inferred a) radial particle flow and b) ratio of electron thermal to particle diffusivity from SOLPS for discharge 162940. The salient observation that $D_e/\chi_e \ll 1$ is robust to these broad sensitivity tests.

Since the primary goal of the sensitivity tests was to produce a range of divertor conditions with recycling characteristics bracketing those measured, the impact of the various assumptions on the radial fueling profile has been analyzed. The 2D fueling profiles from all of the SOLPS simulations have been integrated poloidally to give the radial profile of the ion flux (assuming steady state), which is due to a combination of neutral beam fueling and recycling from the walls. The flux-surface integrated radial particle flow is shown in the pedestal region in Fig. 7. The sensitivity of the pedestal profile is rather weak, indicating rather strong resilience in the interpretive results. The ratio of the effective particle diffusivity to the electron thermal diffusivity is also shown in Fig. 7. The D_e/χ_e ratio shows significant relative variation within the pedestal across the SOLPS calculations, varying roughly in the range of $D_e/\chi_e \sim 0.05$ to ~ 0.15 for both discharges. However, even in the extreme cases where the ion flux to both divertors is much higher than is measured (and hence strongest neutral recycling source), this ratio is always low in magnitude. In other words, the result that $D_e/\chi_e < 0.2$ appears to be robust.

5.3 Summary of Edge Modeling Results

Fig. 8 shows a summary of the transport coefficients calculated by SOLPS and UEDGE for the TPT discharges analyzed in this exercise. The standard H-modes all exhibit similar properties: electron heat diffusivities in the range of $0.1 - 0.5 m^2/s$ and particle diffusivities at least an order of magnitude smaller. The wide pedestal QH (WPQH) mode (DIII-D 163518) exhibits somewhat higher electron heat diffusivity, as may be expected for a broader transport barrier with weaker gradients. Another notable outlier is DIII-D 174092 which was fueled by pellets that penetrate inside the pedestal. This additional particle source increases the particle diffusivity to a level distinctly higher than the other discharges, producing the only scenario with D_e approaching χ_e. Indeed, the prospects for such behavior motivated the selection of this discharge for the TPT. For the remaining discharges, the relation $D_e \ll \chi_e$ firmly holds, pointing to transport mechanisms that are consistent with this feature, as described below.

Similar to other results described in this report, SOLPS modeling for NSTX 129038 found $D_e \sim 0.1 \times \chi_e$ as reported in Ref [11]. Subsequent nonlinear ETG simulations with GS2 (unpublished) found experimentally relevant heat transport levels [12].

We note that JET-ILW 92432 could not be modeled due to nuances of the divertor tile configuration. We also note challenges in modeling the wide pedestal QH mode, for which the separatrix ion temperature is ~ 1.5 keV—far outside the typical edge parameter regime of more conventional H-modes. Despite these challenges, substantial progress was made, resulting in the calculations shown in Fig. 8. The resulting UEDGE simulation, however, was not able to closely match the pedestal density profile, resulting, potentially, in an underestimate of the pedestal particle source. Further refinements will be pursued in the future.

In summary, a large disparity in the magnitude of the transport coefficients, namely $D_e/\chi_e \ll 1$, persists over a large range of discharges in two separate codes and is resilient to extensive variations in input parameters. We consider this rather conclusive demonstration to be a major finding of this exercise. Physical implications will be discussed below.

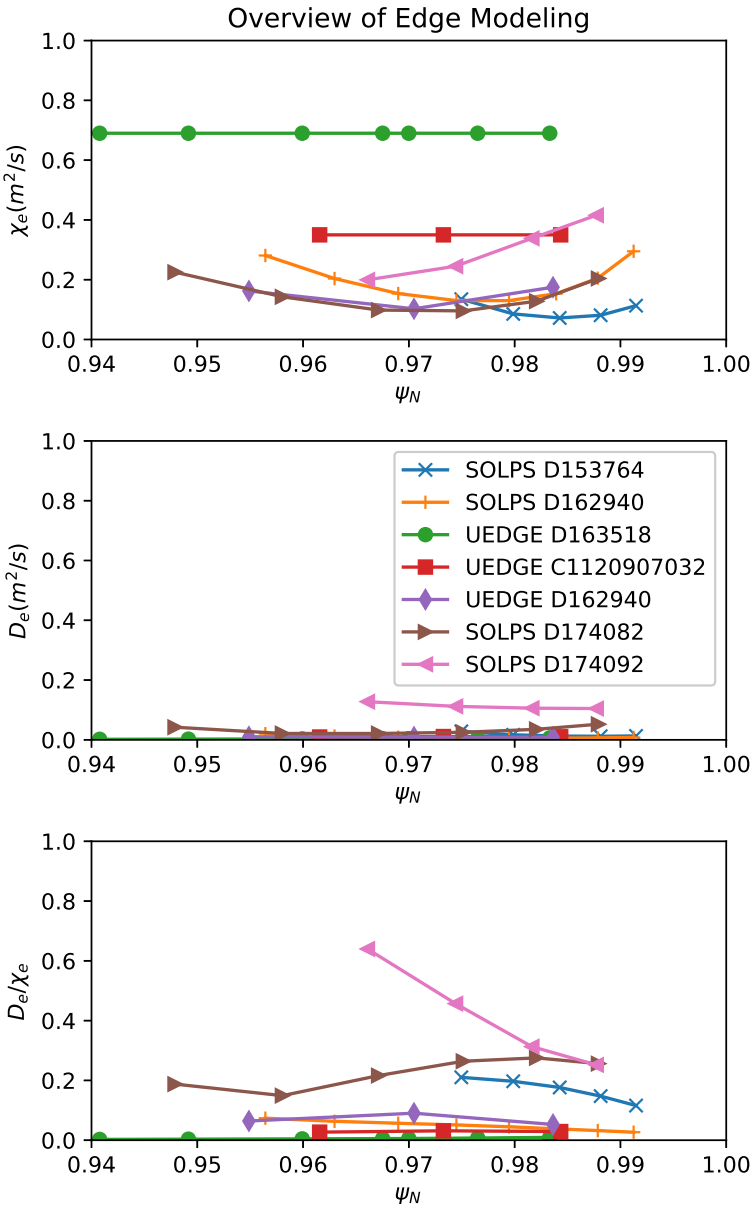

Figure 8: χ_e, D_e, and the ratio of the two for pedestals in six discharges. $D_e/\chi_e \ll 1$ for all cases except DIII-D 174092 where pellets are used to increase the particle source inside the pedestal.

6 Overview of gyrokinetic transport calculations

The edge modeling described in the previous section provides estimates of heat and particle transport coefficients for comparison with gyrokinetic simulations. In this section we detail such comparisons for each discharge in the TPT. We preface this presentation with some discussion of uncertainties.

The total heat flux through the pedestal is a fairly well-constrained quantity that can be arrived at with standard calculations of heating power and radiation. The main uncertainty

in the heat channel is the relative portion of the transport in the ion and electron channels. In the edge modeling, a roughly equal distribution has generally been assumed.

The particle source is subject to more uncertainty than the heat channel. Although the use of SOLPS and UEDGE—two powerful and well-established edge codes—represents the state of the art, substantial uncertainties remain. For the purposes of this exercise, we propose a rough factor of two uncertainty in these calculations (recall Fig. 7).

Even given such uncertainties, we consider the general observation $D_e \ll \chi_e$, consistently found in the edge modeling, to be robust. This places a strong constraint on the mechanisms that can contribute to the pedestal heat transport [8].

There are also substantial uncertainties inherent in the gyrokinetic simulations. Notably, tokamak turbulent transport is notoriously stiff—i.e., sensitive to small changes in background gradients. As described below, we consistently find transport levels from gyrokinetic simulations that are in the experimentally relevant range when allowing for moderate variation of input gradients. Notably, we very rarely find heat transport levels far in excess of the experimental values. When discrepancies are observed, they generally fall in the direction of underpredicting the transport and can often be resolved with moderate variations to background gradients. For the purposes of this exercise, we consider 20-30% variations of gradients to be reasonable. It should be emphasized that this level of agreement between simulations and experiment is very encouraging; it suggests that the inverse problem—predicting profiles from sources—is very likely to be successful once such calculations become accessible via some combination of reduced models and/or continued advances in computational power.

In many cases, parameter variations are carried out to improve agreement. However, given the breadth of this exercises and limited resources (both workforce and computational), such extensive probing was not feasible for all discharges. In this TPT, we consider simulated transport levels within a factor of a few (2-4) of the experimental level to suggest that a given transport mechanisms can be relevant in a given transport channel.

Finally we discuss a few additional limitations on the gyrokinetic simulations. The main transport mechanisms under consideration—MTM, ITG/TEM, ETG, and KBM—make varying computational demands. ETG, which resides at small enough scales to be treated with local flux tube simulations, is the least demanding. Such simulations have been carried out for all discharges of interest. ITG turbulence resides at ion scales, often requiring a numerically demanding global treatment. Such simulations have been carried out in the two discharges where such turbulence appears to be active. MTM turbulence is challenging to model due to its electromagnetic nature and propensity for small radial scales. Although we find near-conclusive evidence (based on comparisons of linear frequencies with fluctuation data) for MTM activity in several discharges, we have only undertake nonlinear simulations in DIII-D shot 153764 (these simulations are described in Ref. [8]). KBM is typically not tractable with gyrokinetics due to its explosive growth beyond its instability threshold. Consequently, our considerations of KBM fluctuations are based entirely on inferences from linear information.

6.1 DIII-D 153764

Detailed analysis of the gyrokinetic simulations for DIII-D discharge 153764 are reported in Ref. [8]. Here we briefly summarize some important results and, additionally, report on

particle transport levels for the first time.

Heat transport levels from GENE simulations of ETG, MTM, and neoclassical are shown in Fig. 9 in comparison with the experimental transport level. The multiple points represent extensive sensitivity tests of ETG and MTM fluctuations, both of which produce meaningful transport levels. Comparisons between SOLPS and GENE particle transport are shown in Fig. 10. Neoclassical and MTM both exhibit experimentally relevant particle transport levels, while ETG particle transport remains quite low even with increased density gradients.

As described in previous reports, MTM fluctuations find close agreement with frequency bands identified in magnetic spectrograms (see Sec. 7 for further discussion). Moreover, the inter-ELM profile evolution is also consistent with MTM; as described in Ref. [8], the fluctuations correlate with saturation of the electron temperature profile but not the density, impurity density, or ion temperature profiles. The low ratio of D_e/χ_e is also consistent with MTM and ETG. Consequently, we conclude that ETG and MTM are the dominant heat transport mechanisms. Within uncertainties, neoclassical and MTM can plausibly account for the particle transport. Additional mechanisms like KBM cannot be ruled out in the particle channel.

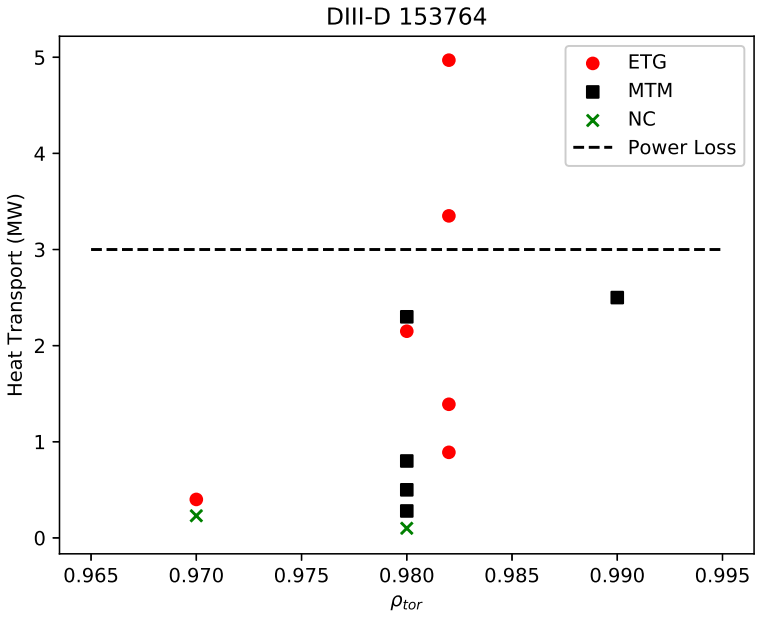

Figure 9: Heat transport from GENE simulations of DIII-D 153764 for nonlinear MTM (black symbols), ETG (red symbols), and neoclassical (green symbols). Both ETG and MTM are found to produce experimentally relevant transport levels. The various points denote extensive sensitivity tests.

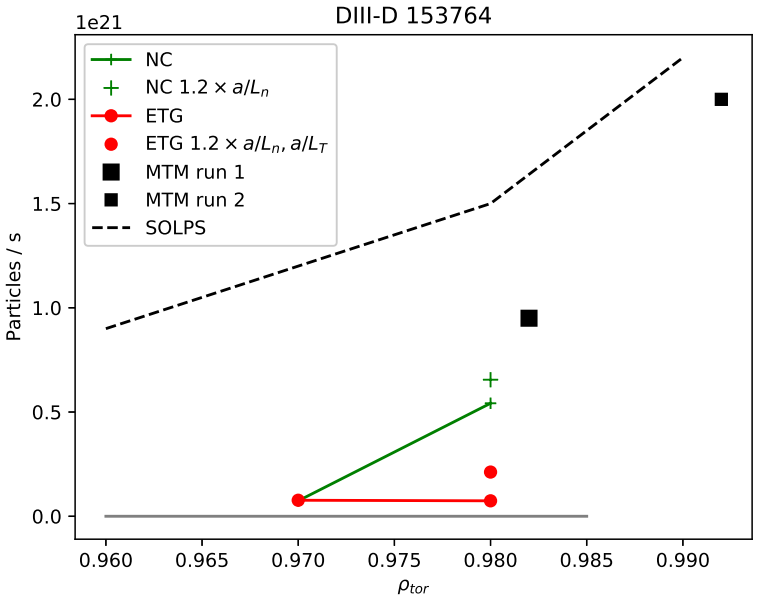

Figure 10: Particle transport (DIII-D 153764) as modeled with SOLPS (black dashed line) and GENE simulations of MTM (black symbols), ETG (red symbols), and neoclassical (green symbols).

6.2 JET-ILW 92432

Gyrokinetic simulations for JET-ILW discharge 92432 are described in detail in Ref. [7]. Heat transport levels from GENE simulations of ETG, ITG, and neoclassical are shown in Figs. 11 and 12 for JET-ILW 92432. As seen in these figures, the heat transport levels closely match the inter-ELM power losses with all three mechanisms making substantial contributions. The columns represent sensitivity tests of impurity content and background gradients.

The particle transport is shown in Fig. 13. Notably, the simulations indicate that ITG turbulence can produce a particle pinch of the same magnitude (but opposite sign) of the neoclassical particle transport. If this inward particle transport is attributed entirely to a pinch (i.e. no contribution from diffusion), the corresponding pinch velocity is $\sim 0.2 m/s$. Sensitivity tests indicate that the ITG particle flux can shift from negative to near-zero with a 5% increase in the density gradient, suggesting close proximity to the point of balanced pinch and diffusion for ITG. These observations suggest that ITG could play a significant role in setting the structure of the density pedestal in scenarios where it is active. Unfortunately, no edge modeling was available for comparison for this discharge.

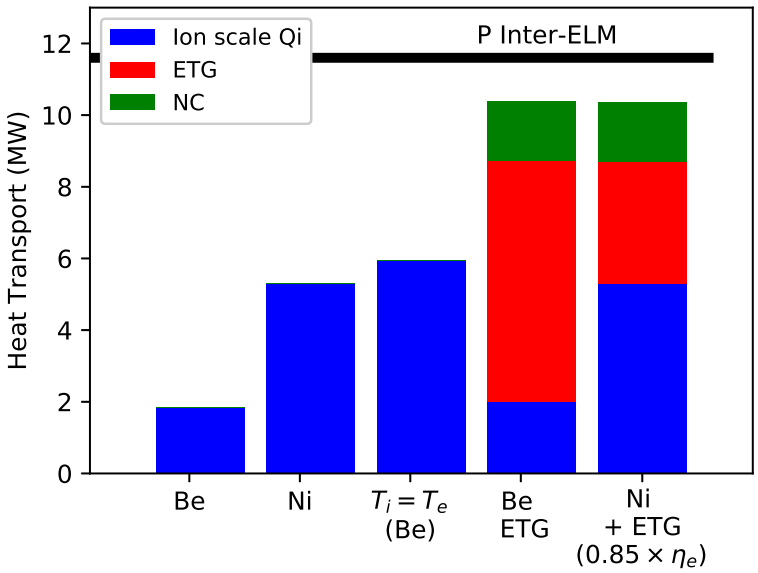

Figure 11: Heat transport from GENE gyrokinetic simulations (JET-ILW 92432) radially averaged over the pedestal. The first three columns illustrate the sensitivities of the ITG turbulence to impurities (main impurity species: fist column beryllium and second column nickel) and ion temperature (first column uses T_i inferred from charge exchange and the second column uses $T_i = T_e$). The final two columns show the sum of transport from ion scale ITG, electron scale ETG, and neoclassical, demonstrating two plausible combinations that reproduce experimental power balance.

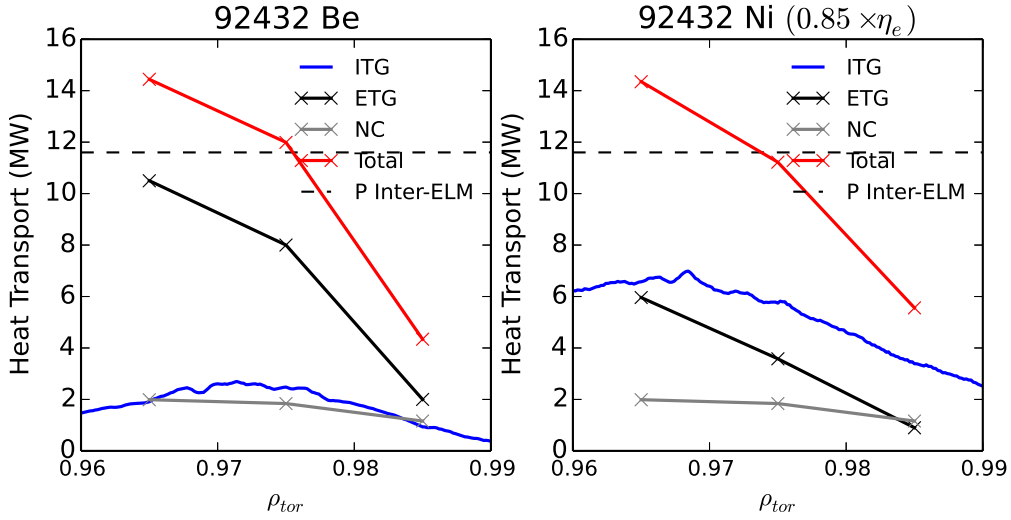

Figure 12: The radial dependence of the heat transport for JET-ILW 92432. The simulations match the experimental level at $\rho_{tor} = 0.965$ (approaching the pedestal top), and $\rho_{tor} = 0.975$ (steep gradient region). The transport is somewhat lower than the experimental level nearer to the separatrix $\rho_{tor} = 0.985$.

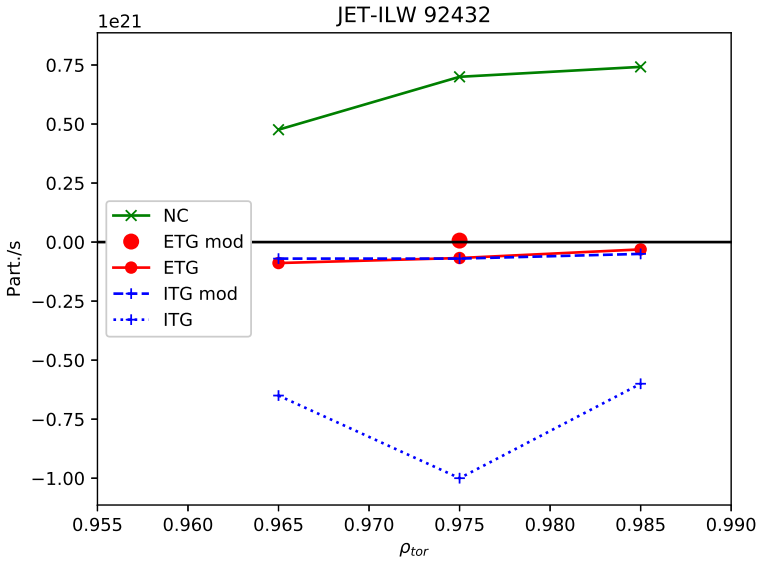

Figure 13: Particle transport from ITG turbulence, ETG turbulence, and neoclassical for JET-ILW 92432. Two ITG simulations are shown with (1) the nominal profiles and (2) modified profiles that increase the density gradient by about 5%. In the former case, the ITG particle pinch is comparable in magnitude (but opposite in sign) to the neoclassical transport.

6.3 DIII-D 162940

DIII-D discharge 162940 was selected for comparisons between both edge (SOLPS and UEDGE) and gyrokinetic (GENE and CGYRO) codes. Both the edge codes and gyrokinetic codes find good agreement on transport quantities as shown in Figs. 3 and 14. Fig. 14 shows heat fluxes from ETG simulations and neoclassical simulations. The GENE results are $\sim 20\%$ higher than CGYRO results. We consider this to be good agreement for a preliminary comparison. Careful comparisons are underway to resolve this minor difference. The ETG transport is at relevant levels when the background gradients are modified within uncertainties ($1.2 \times a/L_T$ and $0.8 \times a/L_n$). Substantial transport is also likely produced by MTM as described below in Sec. 7, where fluctuation data is compared with GENE simulations.

Particle transport from ETG and neoclassical is shown in Fig. 15. Once again, neoclassical produces relevant levels, while ETG is quite small. Additional particle transport mechanisms (e.g. KBM or MTM) are likely necessary in the particle channel.

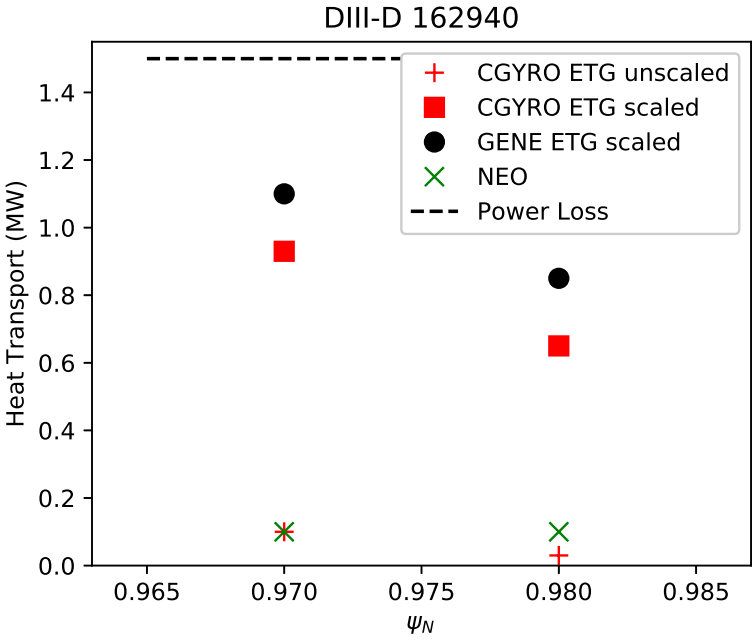

Figure 14: Heat transport calculated by CGYRO, GENE and NEO for DIII-D 162940. The higher transport levels correspond to simulations with temperature gradients increased by a factor of 1.2 and density gradients decreased by a factor of 0.8, suggesting that ETG is near its nonlinear threshold. The modified gradients produce experimentally relevant transport levels. Good agreement is found between GENE and CGYRO for these cases (an ongoing benchmarking exercise is investigating the small remaining discrepancies). Linear GENE simulations of MTM are found to correspond closely to detailed frequency measurements (as described in Sec. 7), suggesting that MTM is also an important transport mechanism for this discharge.

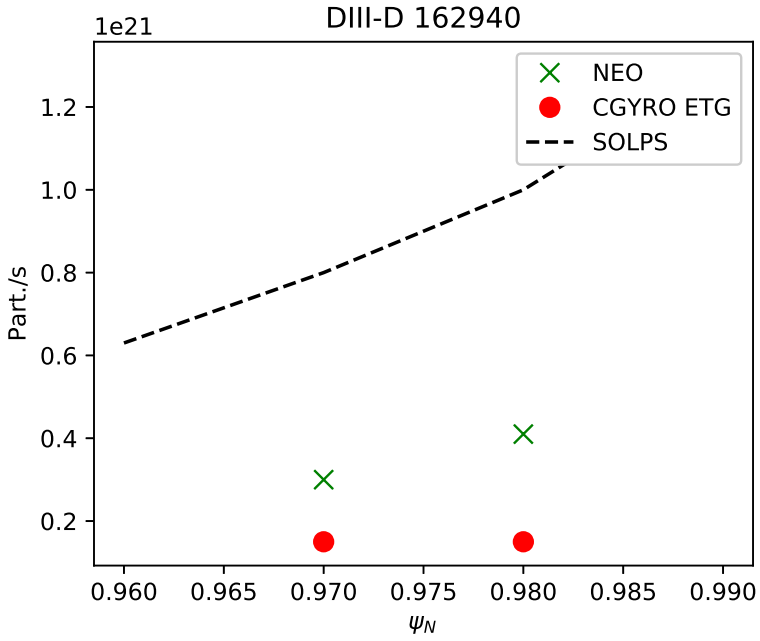

Figure 15: Particle transport for DIII-D 162940 as modeled with SOLPS (dashed line) and CGYRO/NEO (red/gree symbols).

6.4 C-Mod 1120907032

The GENE results for this I-mode discharge are reported in Ref. [21]. Comparisons of heat transport are shown in Fig. 16. ETG easily accounts for the heat transport in the steep gradient region ($\rho_{tor} = 0.98$). The heat transport is underpredicted at 0.97 even with increased drive for ETG. At ion scales, the dominant mode is an impurity branch ITG mode. The remaining discrepancy could plausibly be resolved with modestly higher ITG drive in this region.

Particle transport is shown in Fig. 17 with reasonable agreement between gyrokinetics and UEDGE. Neoclassical transport is close to the UEDGE prediction at both locations while ETG and ITG both produce outward transport at the pedestal top and pinches in the steep gradient region. The ETG and ITG pinches correspond to $v \sim 0.2m/s$ (attributing the flux entirely to pinch and no diffusion).

Notably, UEDGE predicts a small ratio of D_e/χ_e for this discharge, which is consistent with the transport mechanisms identified here (ITG and ETG) but not with the resistive ballooning turbulence proposed elsewhere.

One appealing feature of I-mode is that it maintains an ELM-free state without accumulation of impurities. Consequently, we have also examined impurity transport from the ITG turbulence for this discharge. This was accomplished by a series of gyrokinetic simulations varying background impurity profiles. Results are shown in Fig. 18, demonstrating excellent agreement between the predicted impurity confinement time and that determined experimentally in laser blow off experiments [20].

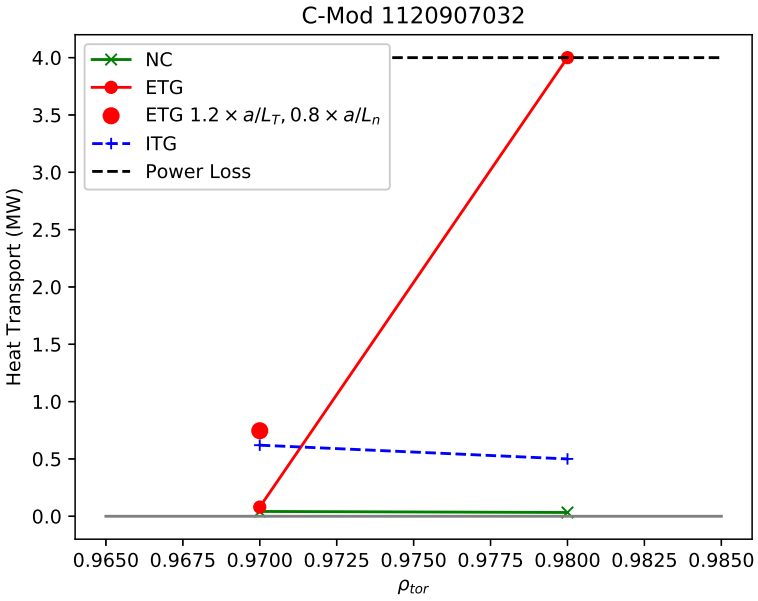

Figure 16: Heat transport from GENE simulations (C-Mod I-mode) of ion scale ITG turbulence (blue symbols), electron scale ETG turbulence (red symbols), and neoclassical (green symbols). Agreement is excellent in the mid-pedestal while GENE underpredicts the transport toward the pedestal top. Sensitivity tests are shown for the ETG turbulence.

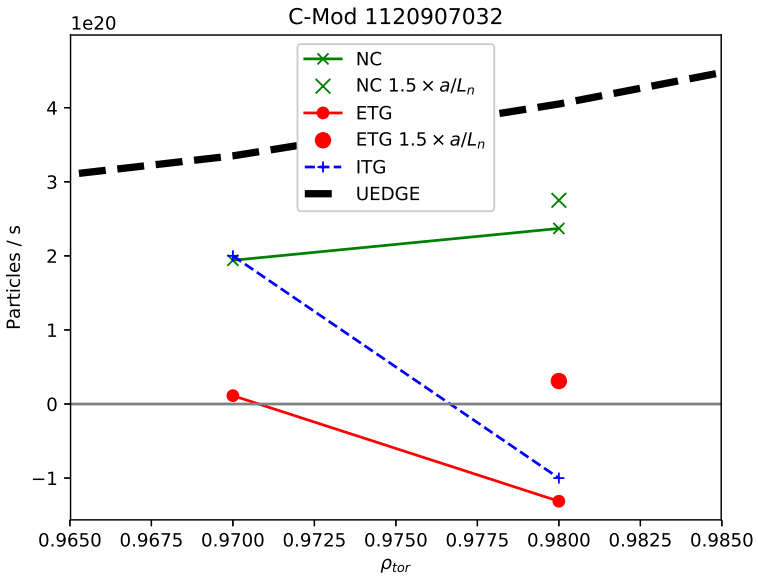

Figure 17: Particle transport (C-Mod I-mode) as modeled with UEDGE (black dashed line) and GENE simulations of ITG (blue symbols), ETG (red symbols), and neoclassical (green symbols).

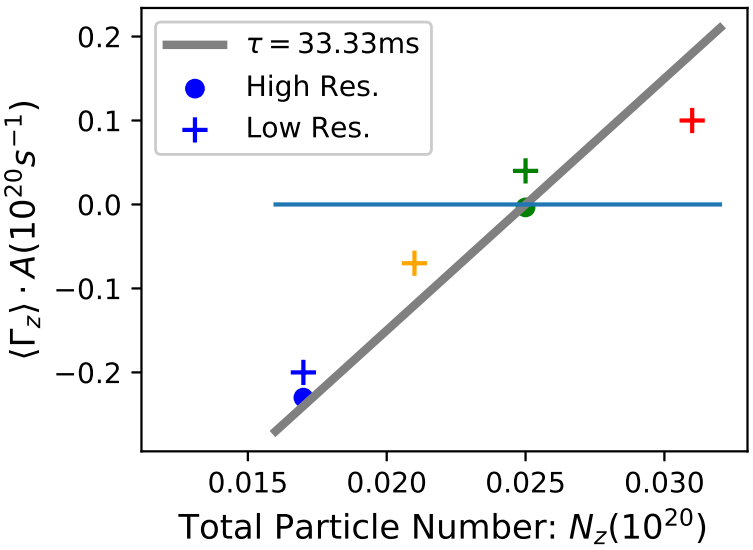

Figure 18: Plot of impurity particle loss rate versus total impurity particle number. The colors of the symbols represent simulations with different impurity gradients. The slope represents the inverse of the impurity confinement time. A line representing t=33 ms is shown for reference. High resolution simulations (n=3-189 with hyperdiffusion) are shown with solid circles and lower- resolution simulations (n=4-60 without hyperdiffusion) are shown with plus symbols, demonstrating that the prediction of impurity confinement time is insensitive to the details of the ky spectrum and, presumably, cross-scale interaction.

6.5 DIII-D 163518

For this wide pedestal QH mode, a local nonlinear GENE simulation at $\rho_{tor} = 0.95$ exhibits many connections with experimental observations. In combination with neoclassical transport, the heat transport closely matches the experimental level as shown in Fig. 19. The frequency spectrum from this simulation also qualitatively matches distinctive features of the BES spectrum as described below in Sec. 7.

The particle transport from both turbulence and neoclassical substantially exceeds the UEDGE prediction as shown in Fig. 20. This may be a reflection of a weak particle source, which facilitates a broadening of the pedestal from low level particle transport mechanisms. Alternatively, the particle source predicted by UEDGE may be too low due to an as-yet-unresolved difference between the UEDGE density profile and the experimental profile.

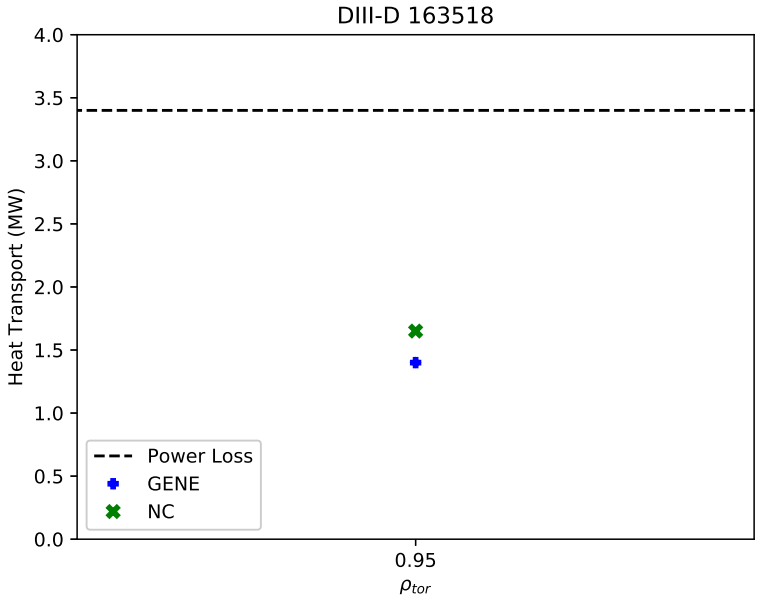

Figure 19: Heat transport from GENE simulations of ion scale turbulence (blue symbol) and neoclassical (green symbol) for DIII-D shot 163518 (wide pedestal QH mode).

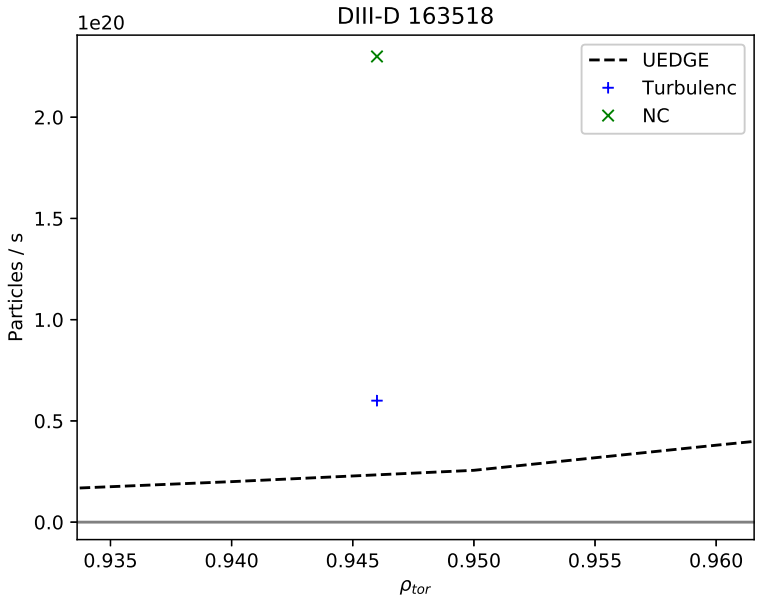

Figure 20: Particle transport (DIII-D 163518) as modeled with UEDGE (black dashed line) and GENE simulations of ion scale turbulent transport (blue symbol) and neoclassical (green symbol). The UEDGE calculation may underpredict the particle source since the density profile is higher than the experimental profile.

6.6 DIII-D 174082 and 174092

GENE simulations for these discharges have been targeted at ETG and linear MTM. The nonlinear ETG achieves relatively modest, though not negligible, transport levels even with

modified gradients (1.2× and 0.8× for temperature and density gradients, respectively). Likewise, neoclassical simulations exhibit small yet non-negligible transport. An additional heat transport mechanism is likely necessary. MTM is the most plausible candidate. Similar to other discharges with available magnetic fluctuations, MTM frequencies find close matches with the magnetic spectrogram as discussed in Sec. 7.

Particle transport from ETG and neoclassical have been studied also for 174082 as shown in Fig. 22. These transport mechanisms produce particle fluxes well below the edge modeling predictions. As discussed above in Sec. 5, 174092 is the only discharge where particle diffusivity approaches heat diffusivity (due to pellet injection). Work is ongoing to identify the relevant transport mechanisms. In addition to potentially different transport mechanisms, the change may be manifest simply in the inter-ELM profile evolution. The ELM frequency for this discharge is very high and, based on available data, it is unclear whether the inter-ELM profiles exhibit any clear saturated phase.

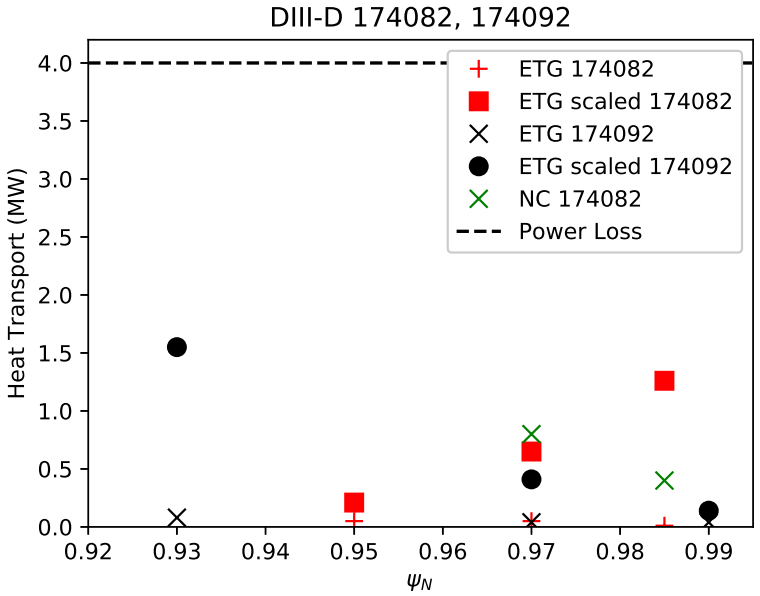

Figure 21: ETG simulations for DIII-D discharges 174082 and 174092. The 'scaled' simulations, using $1.2 \times a/L_T, 0.8 \times a/L_n$, produce non-negligible electron heat transport. MTM frequencies correspond closely with fluctuation data, suggesting it is likely also a major contributor to the electron heat transport.

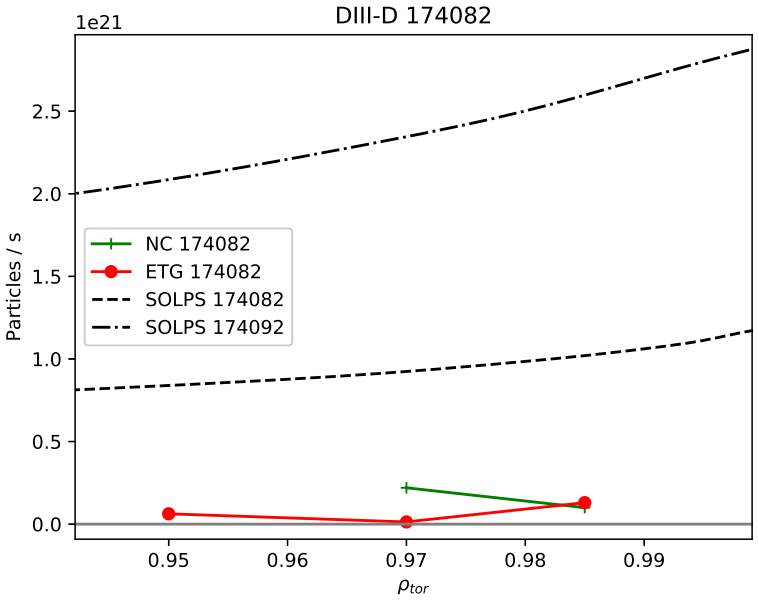

Figure 22: Particle transport (DIII-D 174082 and 174092) as modeled with SOLPS (black lines) and GENE simulations of ETG and neoclassical.

7 Comparisons with Fluctuation Data

Table 2: Summary of fluctuation data used for comparisons with GENE.

Device	Discharge #	Diagnostics
DIII-D	153764	Magnetic probes, BES
DIII-D	162940	Magnetic probes
DIII-D	163518	BES
DIII-D	174082	Magnetic probes, BES

Table 2 summarizes the fluctuation data used for comparison with GENE simulations. We first discuss the BES frequency spectrum for the wide pedestal QH mode in comparison with that from a nonlinear GENE simulations shown in Fig. 23. The two spectra exhibit several features in common. Most notably, both spectra exhibit two distinct frequency branches with a transition at $k_\theta \sim 0.1 cm^{-1}$. The spectra do not, however, agree on the magnitude of the frequency branches. The GENE spectrum appears to be shifted by $\sim 100 - 200 kHz$ in comparison with the BES spectrum. This may be due to a Doppler shift that is not accounted for in GENE and is under further investigation. The high-k, high frequency branch results from TEM turbulence. Notably, the low-k branch corresponds to a region of linear stability. Work is ongoing to better understand the underlying phyics of this turbulence.

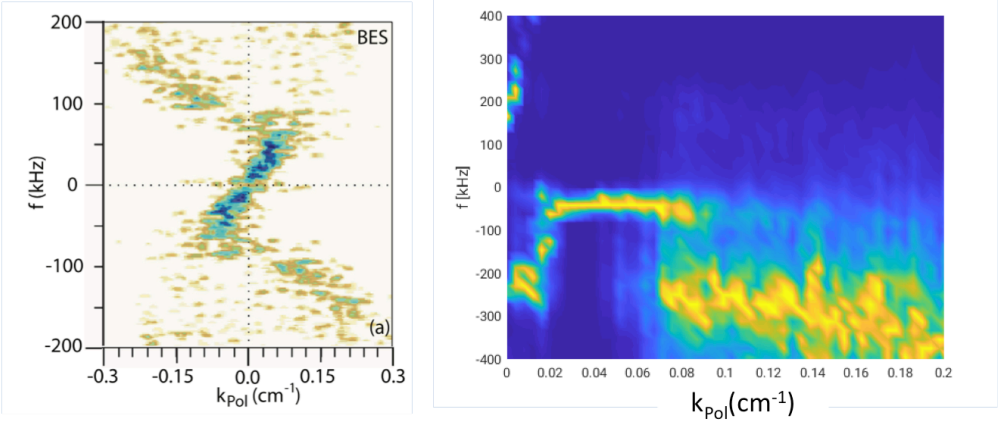

Figure 23: Frequency spectra of fluctuations diagnosed with BES on DIII-D shot 163518 (wide pedestal QH mode) (left) and GENE turbulence simulations (right). Both x (poloidal wavenumber) and y (frequency) can be directly compared. The GENE simulations quantitatively capture a transition between two classes of fluctuations at $k_\theta \sim 0.1$. The frequencies from the GENE simulations are shifted by $\sim 100 - 200kHz$ in the negative direction with respect to the BES frequencies. (The figure on the left is taken from Ref. [5]).

The remaining comparisons with fluctuation data firmly establish MTM as an important pedestal fluctuation. Perhaps the most striking example is shown in Fig. 24, where the magnetic spectrogram (top) for 162940 is shown in conjunction with linear growth rates (bottom left) and frequencies (bottom right) from GENE simulations. All unstable modes in this range of toroidal n numbers are MTM. The three frequency bands where MTM is unstable correspond almost exactly with bands in the spectrogram.

Similar results are seen for 174082, where the frequencies corresponding to the peaks in the linear growth rates find close matches in the spectrogram as shown in Fig. 25. In this case, however, the MTM are unstable over the whole range. The profile fits used in the GENE simulations, in fact, correspond to a point in time where the spectrogram exhibits broad-band turbulence spanning the two peaks. The peak growth rates are at $n = 3$ and $n = 10$, exhibiting fair agreement (within uncertainties) with the inferred toroidal modes

numbers ($n < 3$ and $n = 5 - 8$) from the magnetic probes.

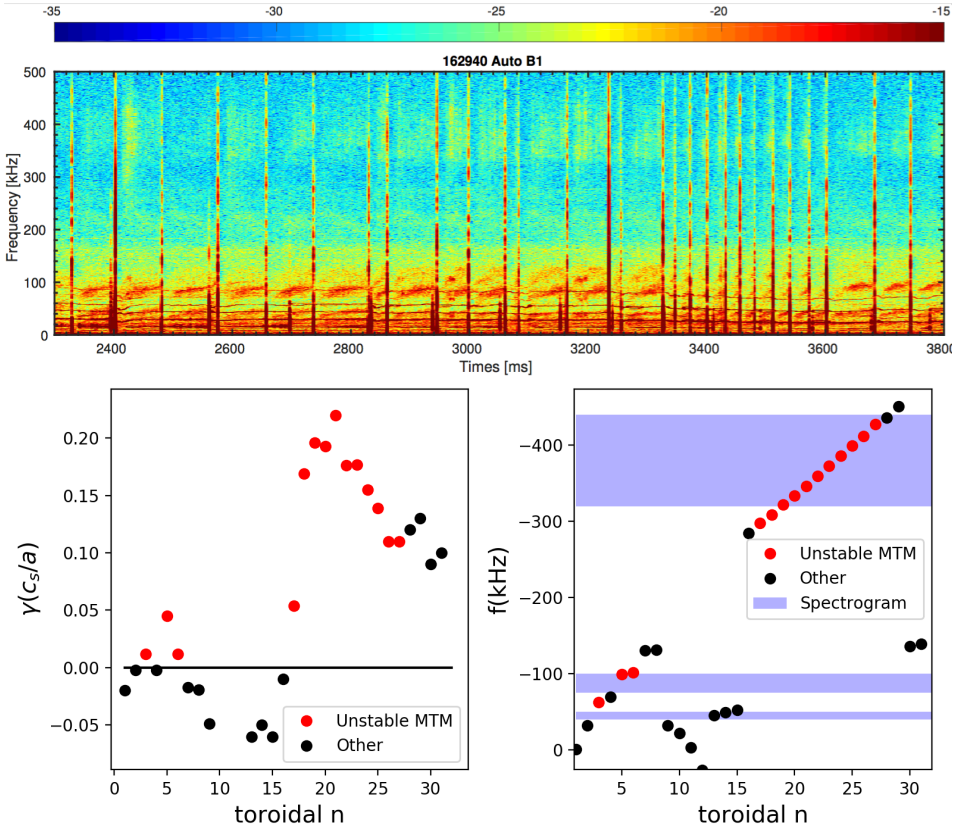

Figure 24: Magnetic spectrogram from magnetic pickup coils for DIII-D shot 162940 (top), spectrum of linear growth rates from GENE simulations (bottom left), and spectrum of frequencies from linear GENE simulations (bottom right). The regions of unstable microtearing modes (red dots) correspond strikingly well with several distinct inter-ELM frequencies bands in the spectrogram.

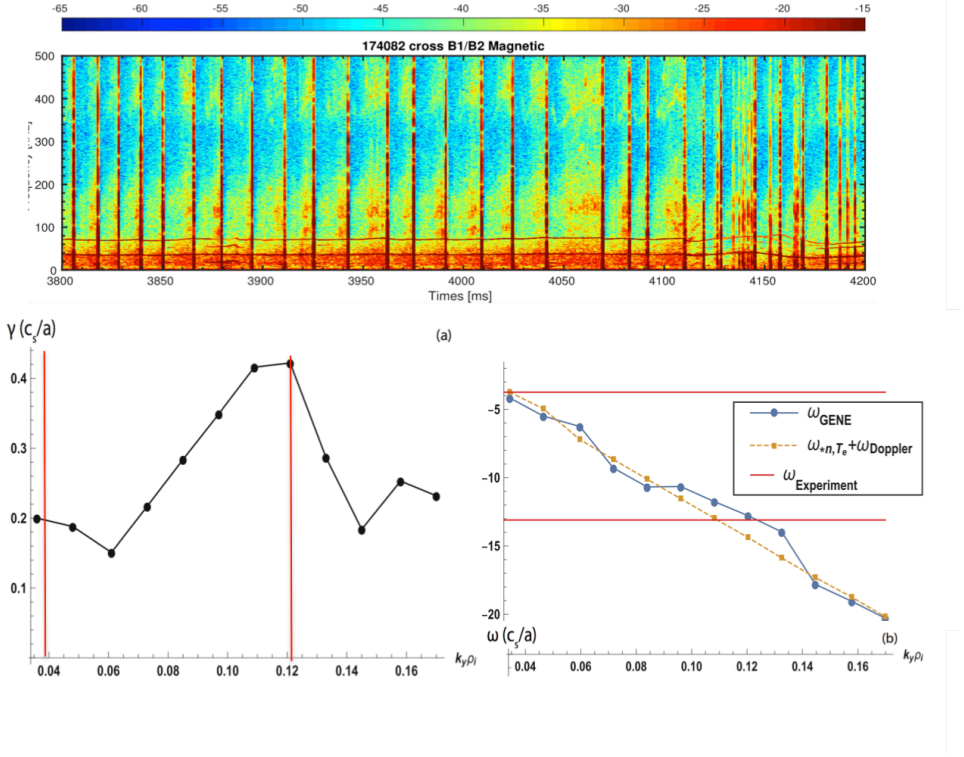

Figure 25: Magnetic spectrogram from magnetic pickup coils for DIII-D shot 174082 (top), spectrum of linear growth rates from GENE simulations (bottom left), and spectrum of frequencies from linear GENE simulations (bottom right). All unstable modes are MTM. The peaks in the MTM growth rates correspond closely to the frequency bands in the magnetic spectrogram. The toroidal n numbers range from 3 to 14.

Comparisons with magnetic spectrograms were also made for DIII-D discharge 153764 and reported in Ref. [8]. Fig. 26 shows the spectrogram (left) along with other relevant frequencies (right). The frequencies are in the electron diamagnetic direction and far exceed the Doppler shift, eliminating any ion-direction mode (e.g. KBM or ITG) from consideration. GENE simulations find MTM at discrete toroidal mode numbers, consistent with the spectrogram. The toroidal mode numbers where MTM are unstable vary sensitively to the details of the background equilibrium. Variations of the background equilibrium with decreased magnetic shear find MTM instabilities in reasonable agreement with the spectrogram, as described in Ref. [8].

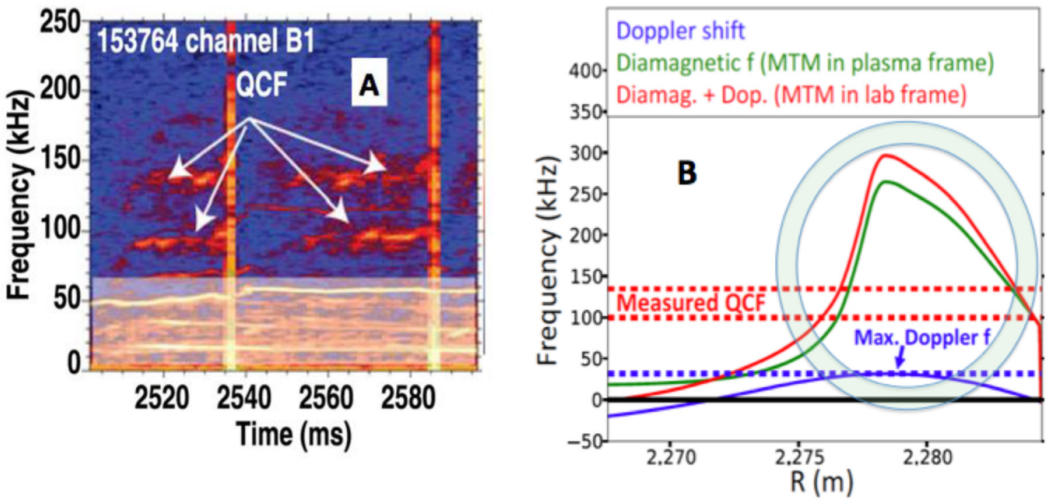

Figure 26: DIII-D shot 153674. (A) Magnetic spectrogram of the experimentally observed fluctuations (taken from Ref. [9]), showing measured QCF and nonlinear simulation frequencies (B) from experimental profiles, and frequencies f for: Doppler shift ($\omega_{E\times B}$), ω_e, and the QCF. The circle shows the experimentally inferred maximum amplitude position of the fluctuation. This figure is borrowed from Ref. [8].

BES data is additionally available for 174082 but strikingly shows no signal, indicating a very low density fluctuation level (roughly estimated to be $\delta n/n < 0.1\%$). This is also consistent with MTM, which is associated with a relatively low density fluctuations in comparison with magnetic fluctuation level.

8 Summary of Major Results

The major results regarding transport are summarized in Fig. 27, which shows the transport coefficients for the discharges studied in the TPT. The curves represent several points in the pedestal as calculated for the various discharges with SOLPS or UEDGE. The other symbols represent the GENE simulation results for neoclassical and the various turbulent mechanisms. The gray diagonal band represents the region accessible to MHD modes like KBM based on basic analytical considerations and GENE simulations. The teal symbols correspond to linear GENE simulations of KBM, situated on this plot by fixing the particle diffusivity (central cluster) or heat diffusivity (upper right cluster) to meaningful levels. Green x's denote neoclassical simulations, blue +'s ITG simulations, red dots ETG simulations, and black squares MTM simulations. All heat diffusivities are for electrons with the exception of neoclassical and ITG, for which ion heat diffusivity is shown. All particle diffusivities are for electrons. Particle diffusivities below 1.0×10^{-4} (including negative values) are shown on this plot at 1.0×10^{-4}.

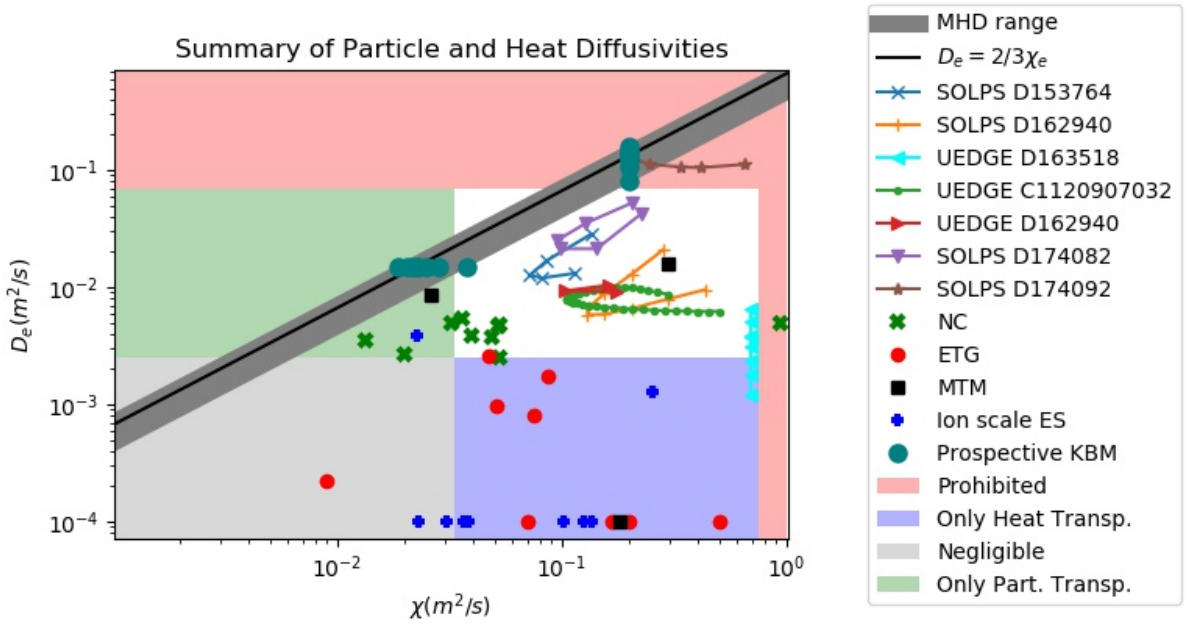

Figure 27: Summary of the transport coefficients for the discharges studied in the TPT. The curves represent several points in the pedestal as calculated for the various discharges with SOLPS or UEDGE. The other symbols represent the GENE, CGYRO, and NEO results for various instabilities and neoclassical. The gray diagonal band represents the region accessible to MHD modes like KBM based on basic analytical considerations. The teal symbols represent GENE simulations of KBM, situated on this plot by pinning the particle diffusivity (central band) or heat diffusivity (upper right band) to a given level. Green x's denote neoclassical simulations, blue +'s ITG simulations, red dots ETG simulations, and black squares MTM simulations. All heat diffusivities are for electrons with the exception of neoclassical and ITG, which represent ions. All particle diffusivities are for electrons. Particle diffusivities below 1.0×10^{-4} (including negative values) are shown on this plot at 1.0×10^{-4}.

Several notable observations can be made. First, all the conventional H-modes lie in a fairly tight cluster with $0.1 < \chi_e < 0.5$ and $5 \times 10^{-3} < D_e < 5 \times 10^{-2}$. Outliers are the WPQH, which has high heat diffusivity, as may be expected for a mode with higher transport exploited to widen the pedestal. Another outlier is DIII-D 174092, which apparently succeeds in increasing the particle diffusivity via pellet injection. The neoclassical transport consistently lies in a region of small yet non-negligible transport in both the particle and heat channels. ETG, MTM, and ITG consistently produce relevant levels of heat transport. In multiple cases the combination of ETG and neoclassical is not sufficient to fully account for power balance even with somewhat modified gradients to enhance ETG transport. In such cases, MTM is the most plausible candidate to further account for the heat flux. This conclusion is based on the $D_e/\chi_e \ll 1$ constraint, the nonlinear simulations of DIII-D 153764, and the close match between GENE simulations and magnetic spectrograms from several discharges.

ITG and ETG generally produce small or negative particle transport but can in some cases approach relevant levels of particle diffusivity. MTM can produce transport levels that

are simultaneously relevant in both channels (note the black square solidly in the white region). The gray band denoting the range of MHD-like fluctuations indicates that such mechanisms, if active, cannot simultaneously dominate both transport channels, and in fact must be limited to the particle channel.

The major conclusions of this TPT are as follows:

- Edge transport barriers typically lie in a regime in which heat diffusivity far exceeds particle diffusivity: $D_e/\chi_e \ll 1$. This conclusion was robust to extensive SOLPS sensitivity tests.

- ETG and MTM are important mechanisms for electron heat transport and one or both will generally be major contributors to χ_e.

- In addition to its transport signature, which is consistent with $D_e/\chi_e \ll 1$, MTM activity is further established, perhaps incontrovertibly, by the close quantitative agreement between distinctive bands in magnetic spectrograms and corresponding bands of unstable MTM in gyrokinetic simulations. This is now established over several discharges.

- Neoclassical transport in electron particle and ion heat channels is consistently at levels that are not negligible, but remains somewhat smaller than edge modeling predictions.

- MHD modes, if active, cannot simultaneously account for all transport in both particle and heat channels and in fact must be limited to the particle channel.

- ITG and ETG are observed in some cases to produce pinch velocities of up to $\sim 0.2 m/s$ (attributing all flux to pinch and no diffusion).

- Neoclassical, MTM, ETG, and ITG can all produce relevant particle transport levels (the latter two in either positive or negative directions). Within uncertainties, they can plausibly account for all particle transport. Generally, however, these mechanisms are found to collectively produce particle transport somewhat below the edge modeling predictions. This suggests that an additional particle transport mechanism, like KBM, may be necessary.

Acknowledgements.– This research used resources of the National Energy Research Scientific Computing Center, a DOE Office of Science User Facility. We also acknowledge the CINECA award under the ISCRA initiative, for the availability of high performance computing resources and support. This work was supported by U.S. DOE Contract No. DE-FG02-04ER54742; U.S. DOE Office of Fusion Energy Sciences Scientific Discovery through Advanced Computing (SciDAC) program under Award Numbers DE-SC0018429 and DE-SC0018148; and General Atomics award number 4500076923. This material is based upon work supported by the U.S. Department of Energy, Office of Science, Office of Fusion Energy Sciences, using the DIII-D National Fusion Facility, a DOE Office of Science user facility, under Award DE-FC02-04ER54698.

References

[1] Jenko F., Dorland W., Kotschenreuther M. and Rogers B.N. 2000 Phys. Plasmas 7 1904

[2] Goerler T., Lapillonne X., Brunner S., Dannert T., Jenko F., Merz F. and Told D. 2011 J. Comput. Phys. 230 7053

[3] J. Candy, E. A. Belli, and R. V. Bravenec, J. Comput. Phys. 324, pp. 73–93, 2016.

[4] D.G. Whyte et al 2010 Nucl. Fusion 50 105005

[5] X. Chen et al., Nucl. Fusion, vol. 57, no. 8, p. 086008, Aug. 2017.

[6] P.B. Snyder, R.J. Groebner, A.W. Leonard, T.H. Osborne, and H.R. Wilson, Phys. Plasmas, 16:056118, 2009.

[7] D. R. Hatch, M. Kotschenreuther, S. M. Mahajan, G. Merlo, A. R. Field, C. Giroud, J. C. Hillesheim, C. F. Maggi, C. Perez von Thun, C. M. Roach, S. Saarelma, and JET Contributors, Nucl. Fusion, vol. 59, p. 086056, 2019.

[8] M. Kotschenreuther, X. Liu, D. R. Hatch, S. Mahajan, L. Zheng, A. Diallo, R. Groebner, the DIII-D TEAM, J. C. Hillesheim, C. F. Maggi, C. Giroud, F. Koechl, V. Parail, S. Saarelma, E. Solano, A. Chankin, and JET Contributors, Nucl. Fusion, vol. 59, p. 096001, 2019.

[9] A. Diallo et al. Phys. Plasmas, vol. 22, no. 5, p. 056111, May 2015.

[10] D. R. Hatch, M. Kotschenreuther, S. Mahajan, P. Valanju, and X. Liu, Nucl. Fusion, vol. 57, p. 036020, 2017.

[11] J. Canik et al., Phys. Plasmas, 18, 056118 (2011).

[12] J. Canik, Transport Taskforce Meeting 2014, San Antonio, TX.

[13] R. Schneider, et al, Contrib. Plasma Phys. 46 (2006) 3.

[14] B.J. Braams, Contrib. Plasma Phys. 36 (1996) 276.

[15] D. Reiter, M. Baelmans, P. Boerner, Fusion Sci. Techol. 47 (2005) 172 and www.eirene.de

[16] S. Wiesen, et al, J. Nucl. Mat. 463 (2015) 480.

[17] A.W. Leonard et al, J. Nucl. Mat. 390-391 (2009) 470.

[18] J. D. Callen, J. M. Canik, and S. P. Smith, Phys. Rev. Lett., vol. 108, no. 24, p. 245003, Jun. 2012.

[19] J. W. Connor, R. J. Hastie, and J. B. Taylor, "Comment on 'Derivation of paleoclassical key hypothesis' [Phys. Plasmas 14, 040701 (2007)]," p. 3.

[20] J.E. Rice, M.L. Reinke, C. Gao, N.T. Howard, M.A. Chilenski, L. Delgado- Aparicio, R.S. Granetz, M.J. Greenwald, A.E. Hubbard, J.W. Hughes, J.H. Irby, Y. Lin, E.S. Marmar, R.T. Mumgaard, S.D. Scott, J.L. Terry, J.R. Walk, A.E. White, D.G. Whyte, S.M. Wolfe and S.J. Wukitch, 2015 Nucl. Fusion 55 033014

[21] X. Liu, PhD Dissertation, University of Texas at Austin, 2018.